https://doi.org/10.5194/egusphere-2025-2610
Preprint. Discussion started: 23 June 2025

Migrating diurnal tide anomalies during QBO disruptions in 2016 and 2020: morphology and mechanism

Shuai Liu[1,2], Guoying Jiang[1,3,4], Bingxian Luo[1,2], Xiao Liu[5], Jiyao Xu[1,3], Yajun Zhu[1,3,4], Wen Yi[6,7]

[1]State Key Laboratory of Solar Activity and Space Weather, National Space Science Center, Chinese Academy of Sciences, Beijing, 100190, China
[2]College of Earth and Planetary Sciences, University of Chinese Academy of Sciences, Beijing, 101408, China
[3]School of Astronomy and Space Science, University of Chinese Academy of Sciences, Beijing, 101408, China
[4]Hainan National Field Science Observation and Research Observatory for Space Weather, Danzhou, Hainan Province, China.
[5]School of Mathematics and Statistics, Henan Normal University, Xinxiang, 453007, China
[6]CAS Key Laboratory of Geospace Environment, Department of Geophysics and Planetary Sciences, University of Science and Technology of China, Hefei, China
[7]CAS Center for Excellence in Comparative Planetology, Anhui Mengcheng Geophysics National Observation and Research Station, University of Science and Technology of China, Hefei, China

Correspondence to: Guoying Jiang (gyjiang@swl.ac.cn) and Bingxian Luo (luobx@nssc.ac.cn)

Abstract. The stratosphere Quasi-Biennial Oscillation (QBO) modulates the migrating diurnal tide (DW1) in mesosphere and lower thermosphere (MLT). DW1 amplitudes are larger during QBO westerly (QBOW) than during easterly (QBOE) phases. Since QBO's discovery in 1953, two rare QBO disruption events occurred in 2016 and 2020. During these events, anomalous westerly winds propagate upward, disrupting normal downward propagation of easterly phase and producing a persistent westerly wind layer. In this study, global responses of DW1 amplitudes and phases in MLT to these QBO disruptions, as well as the excitation sources are investigated, using SABER/TIMED observations, MERRA-2 reanalysis and SD-WACCM-X simulations. Similarity of the DW1 responses to these two events is that DW1 phases and wavelengths exhibit weak responses to these events, whereas the amplitudes show significant responses. Relative to regular QBOE, DW1 amplitudes increase by ~20.5 % at equator and 14.4 % at 30°N/S during the 2016 event, but by only ~6.0 % and 2.0 % during the 2020 event. Water vapour radiative heating, ozone radiative heating and latent heating are enhanced by ~10 %, ~6.6 % and ~22 % relative to QBOE in 2016 event. In 2020, water vapour radiative heating shows a clear increase (~9 %), whereas ozone heating and latent heating remain nearly unchanged to the QBOE. In summary, the simultaneous amplification of water vapour, ozone and latent heating could account for the pronounced DW1 amplitude increase in 2016 event, while the enhancement of water vapour heating may explain the weaker response in 2020 event.

1 Introduction

Atmospheric solar tides are planetary-scale harmonic waves with periods of a solar day. In the mesosphere and lower thermosphere (MLT), solar tides exert significant influences on atmospheric parameters such as wind, temperature, and density

https://doi.org/10.5194/egusphere-2025-2610
Preprint. Discussion started: 23 June 2025

(Chapman & Lindzen, 1980; Xu et al., 2009; Jiang et al., 2010; Smith, 2012). Among these tides, the migrating diurnal tide (DW1) is one of the most prominent components. DW1 in MLT is modulated by external forcings, including the stratosphere Quasi-Biennial Oscillation (QBO, Hagan et al., 1999; Wu et al., 2008; Xu et al., 2009; Oberheide et al., 2009; Mukhtarov et al., 2009; Davis et al., 2013; Gan et al. 2014), El Niño–Southern Oscillation (ENSO, Lieberman et al., 2007; Cen et al., 2022) and 11-year solar cycle response (Singh and Gurubaran, 2017; Sun et al., 2022; Liu et al., 2024a; Liu et al., 2024b). In this work, the impact of QBO is focused.

The QBO dominates the variability of the equatorial stratosphere (~16–50 km), shown as alternating downward propagating easterly wind (so-called QBO easterly phases) and westerly wind (so-called QBO westerly phases), with an averaging period of approximately 28 months (Baldwin et al., 2001). QBO is driven by vertically propagating Kelvin, mixed Rossby gravity waves and small-scale gravity waves (Lindzen and Holton, 1968; Holton and Lindzen, 1972; Baldwin et al., 2001; Ern et al., 2014). It could influence the transport and distribution of trace gases like water vapor and ozone in the troposphere and stratosphere (Schoeberl et al., 2008). During the winter of 2015/16 and 2019/20, two rare stratospheric QBO disruption events occurred, which were found only twice since the record began in 1953. The events are manifested by anomalous westerly winds propagating upward, disrupting normal downward propagation of the easterly phase and producing a persistent westerly wind layer (Newman et al., 2016; Anstey et al., 2021). In 2020 event, the upward westerly wind is so weak that the monthly mean zonal wind is shown as upward easterly wind (e.g. Anstey et al., 2021; Wang et al., 2023). The events are driven by strong extratropical Rossby waves propagating toward the tropics (Kang et al., 2022; Kang and Chun, 2021; Wang et al., 2023). In these two events, the trace gases like ozone and water vapor are also modulated. During the 2016 disruption event, the concentration of trace gases like ozone and water vapor increased in boreal winter (September 2015–March 2016) and subsequently decreased between the tropopause and lower stratosphere. A similar pattern occurred in boreal winter 2019–June 2020, after which concentrations declined (Tweedy et al., 2017; Diallo et al., 2018, 2022).

QBO modulation of diurnal tides has been reported by both ground-based and space-borne observations (Araújo et al., 2017; Davis et al., 2013; Pramitha et al., 2021b; Wu et al., 2008; Dhadly et al., 2018). Mayr and Mengel (2005) reported that the QBO can affect these amplitudes by up to 30% using the Numerical Spectral Model (NSM). Thermosphere, Ionosphere, Mesosphere Energetics and Dynamics/Sounding of the Atmosphere using Broadband Emission Radiometry (TIMED/SABER) observations revealed that the quasi-biennial variability of DW1 could exceed 50% at certain altitudes (Garcia, 2023). The modulation was characterized by larger-than-average diurnal tide amplitudes during the westerly phase of the QBO and smaller-than-average amplitudes during the easterly phase (Vincent et al., 1998; Wu et al., 2008; Xu et al., 2009; Davis et al., 2013; Araújo et al., 2017; Pramitha et al., 2021b; Garcia, 2023).

Recent studies have shown that the diurnal tides were also modulated during the QBO disruption events (Pramitha et al., 2021a; Garcia, 2023; Wang et al., 2024). Pramitha et al. (2021a) first reported the enhancement of the diurnal tides during the 2015/2016 SOBO disruption event using meteor radar over Tirupati (13.63°N, 79.4°E) and linked this enhancement to changes in ozone concentration. Garcia (2023) showed the equatorial response of temperature DW1 to these two disruption events when analysing the QBO modulation to DW1. Wang et al. (2024) reported the weakened mesospheric diurnal tides at mid-

https://doi.org/10.5194/egusphere-2025-2610
Preprint. Discussion started: 23 June 2025

latitude during QBO disruption events, which is observed by a meteor radar chain. They further gave the modulation evidence of gravity wave forcing and solar radiative absorption by subtropical stratospheric ozone revealed by SD-WACCM-X simulations.

These findings raise three questions: (1) In addition to the equatorial peak, temperature DW1 exhibits secondary amplitude maxima at 30°N and 30°S (Xu et al., 2009; Garcia, 2023). Whether the DW1 amplitudes on a global scale show a similar response to the QBO disruption events. (2) Whether the phases and wavelengths of DW1 could be affected by the events. (3) The water vapor radiative heating and latent heating were another source of DW1(Hagan, 1996; Kogure and Liu, 2021). Whether the water vapor radiative heating and latent heating play roles in modulating DW1 during the disruption events.

The present study will focus on the global response feature of DW1 and its excitation sources to QBO disruption events. The response of DW1 amplitudes, phases and wavelengths during the event will be investigated. Moreover, the contribution of excitation sources, including ozone radiative heating, water vapor radiative heating and latent heating variation during the event will be explored. The article is organized as follows: Section 2 introduces TIMED/SABER, SD-WACCM-X, MERRA-2 data and the methodologies to extract the migrating tides. Section 3 presents the response feature of the DW1 to the QBO disruption events revealed by SABER/TIMED observations and SD-WACCM-X simulation results. The possible mechanism of DW1 response to the disruption events is discussed in Section 4. Section 5 presents the summary.

2 Data and methodology

This study employs the dataset of SABER/TIMED observations, SD-WACCM-X simulations and MERRA-2 reanalysis to reveal the feature of DW1 and its excitation sources during QBO disruption events. DW1 amplitude, phase, and wavelength are derived from both SABER/TIMED data and SD-WACCM-X outputs. MERRA-2 reanalysis is used to analyse the contributions of water vapor radiative heating and latent heating to DW1 variability during the QBO disruption events, while SABER/TIMED observations characterize ozone radiative heating. SD-WACCM-X simulations validate the excitation source revealed by the observational datasets.

2.1 SABER/TIMED observations

The TIMED satellite is in a near sun-synchronal orbit with a 73° inclination at about 625 km. The number of orbits observed per day is about 15. SABER, an instrument in the TIMED satellite, is a 10-channel broadband (1.27–17 μm) limb-scanning infrared radiometer. SABER observations of infrared radiance are used to retrieve kinetic temperature, trace gases, etc. In this work, kinetic temperature and ozone observations in level 2 A (L2A) dataset and ozone heating rate in level 2B (L2B) dataset are selected to analyse the DW1 response to QBO disruption events. Kinetic temperature is derived using a full nonlocal thermodynamic equilibrium (non-LTE) inversion algorithm (Mertens et al., 2001; 2004) with the combination of the measured 15 μm CO_2 vertical emission profile and CO_2 concentrations provided by the Whole Atmosphere Community Climate Model (WACCM 3.5.48) described in Garcia et al. (2007). The ozone volume mixing ratio (VMR) is derived from the measured 9.6

https://doi.org/10.5194/egusphere-2025-2610
Preprint. Discussion started: 23 June 2025

μm and 1.27 μm O3 vertical emission profiles (Smith et al., 2013). 9.6 μm O_3 observations cover all local time and 1.27 μm O_3 covers daytime. In this work, the VMR data retrieved from 9.6 μm O_3 is selected. The ozone heating rate is derived from the sum of the heating rates in three bands, including the Hartley band, Huggins band and Chappuis band.

It takes SABER 60 days to sample 24 hours in local time. The data latitudinal coverage every 60 days extends from 53°N to 83°S or 53°S–83°N. Temperature observations taken from version 2.07 data from 2002 to 2019 and version 2.08 data from 2020 to 2023 are used. The details of the version switches could refer to Mlynczak et al. (2022, 2003). The retrieved temperature observations used in this work cover altitudes from approximately 20 km to 105 km. The ozone heating rate data range from 20 km to 50 km.

2.2 SD-WACCM-X

The Whole Atmosphere Community Climate Model with thermosphere–ionosphere eXtension (WACCM-X) is a comprehensive numerical model that could simulate the Earth's atmosphere from the surface up to the upper thermosphere, including the ionosphere. WACCM-X consists of two parts, WACCM4 (Marsh et al., 2013) and Thermosphere-Ionosphere-Electrodynamics General Circulation Model (TIE-GCM, Qian et al., 2014). WACCM4 is based on NCAR Community Atmosphere Model 4 (CAM4, Neale et al., 2013). The WACCM4 contains chemical, physical and dynamical processes in the troposphere, stratosphere, mesosphere, and lower thermosphere. TIE-GCM includes the ionosphere–thermosphere processes (Pedatella, 2022). SD in the SD-WACCM-X means specified dynamics, which is an approach described in Smith et al. (2017). The reanalysis fields from Modern-Era Retrospective analysis for Research and Applications, Version 2 (MERRA-2, Gelaro et al., 2017) data from the surface up to ~50 km are nudged in WACCM-X.

Model parameters are output in 3-hour resolution. The latitude-longitude resolution is 1.9°×2.5°. The model has 145 pressure levels with a varying vertical resolution of ~1.1–1.75 km in the troposphere and stratosphere and ~3.5 km in the mesosphere. In this work, the temperature, zonal wind, temperature tendency due to moist process and long wave heating rate ranging from 2002 to 2022 are selected.

2.3 MERRA-2

MERRA-2 is a reanalysis product from the NASA Global Modeling and Assimilation Office (GMAO) and provides data like wind, temperature, mixing ratio of components, etc. (Gelaro et al., 2017). In this work, the zonal wind, temperature, air density, surface albedo, water vapor mixing ratio and temperature tendency due to moist process range from 2002 to 2023 are selected. The time resolution is 3-hour per day. The spatial resolution is a 2.5°×2.5° latitude-by-longitude grid at 72 model levels from ground to 0.01 hPa.

2.4 Singapore radiosonde QBO index

The QBO index employed in this study is derived from Singapore radiosonde measurements obtained by the Meteorological Service Singapore Upper Air Observatory (station 48698; 1.34°N, 103.89°E; 21 m above mean sea level). The monthly mean

https://doi.org/10.5194/egusphere-2025-2610
Preprint. Discussion started: 23 June 2025

zonal wind data processed by the National Aeronautics and Space Administration/Goddard Space Flight Center (NASA/GSFC) is selected, spanning 2002–2023 at pressure levels between 100 hPa and 10 hPa.

2.5 Water vapor radiative heating rate calculation

Troposphere heating by water vapor absorption of near-infrared radiation is an important excitation source for DW1 (Hagan, 1996; Lieberman et al., 2003). Due to the SABER's observational gap in the troposphere, the MERRA-2 dataset is adopted. In this dataset, temperature, air density, surface albedo, cloud fraction and water vapor mixing ratio (specific humidity) are the variables necessary for the calculation. The heating rate is the sum of clear sky and cloudy sky (Groves et al., 1982):

$$J = (1-k)J_{clear} + kJ_{cloudy} \quad (1)$$

where k is the cloud fraction, J_{clear} and J_{cloudy} are the heating rates of the clear sky and cloudy sky. The calculation equations for clear sky and cloudy sky are given in Appendix A.

2.6 Method for extracting DW1 and data processing

Non-uniform SABER observational data were processed into zonal mean data and used to extract tides. The procedures are introduced briefly as follows. Firstly, the kinetic temperature, ozone mixing ratio and ozone radiative heating rate profiles are interpolated vertically with a 1 km spacing. Profiles of each day are sorted into ascending and descending groups. Secondly, the global temperature and ozone observations at whole heights and in both groups were processed into zonal mean results, covering latitudes from 50°S to 50°N with a resolution of 5°. At a fixed latitude and height, the following equation proposed by Xu et al. (2007) is used to extract the tide from the zonal mean temperature in a 60-day window:

$$\frac{1}{2\pi}\int_0^{2\pi} T(t_{LT},\lambda)d\lambda = \bar{T} + \eta(t-t_0) + \sum_{n=1}^{N} A_n cos(n\omega t_{LT}) + \sum_{n=1}^{N} B_n sin(n\omega t_{LT}) \quad (2)$$

where ω = 2π/24(hour), t_{LT} is the local time, λ is longitude in radians. $\bar{T}$is the 60-day window average of the zonal mean temperature. η describes the linear trend variation in the window. t is the day of the window and t_0 is the center day of the window. The third and fourth term of the right section of the equation denotes the superimposed harmonic signals by four periods migrating tides, including diurnal tide (DW1), semidiurnal tide (SW2), terdiurnal tide (TW3), and 6-h tide (QW4). N in the third term represents four signals and n denotes each signal. The amplitude and phase of each migrating tide are retrieved using $\sqrt{A_n^2 + B_n^2}$ and $arctan(B_n/A_n)$, respectively. The overlapping analyses are obtained by sliding the 60-day window forward in 1-day intervals to obtain the daily values of the wave characteristics. The details of the methods used for data processing and tide extraction could refer to Xu et al. (2007, 2009) and Liu et al. (2024a).

The method for extracting tidal components from ozone heating rates follows Equation 4 in Xu et al. (2010). The methods for tidal extraction from MERRA-2 and SD-WACCM-X differ from those used for SABER due to differences in data structure. Unlike SABER, both MERRA-2 and SD-WACCM-X provide spatially uniform data with a 3-hour temporal resolution. As a result, a two-dimensional Fast Fourier Transform (2D-FFT) is directly applied to extract daily DW1 amplitudes and phases of temperature, water vapor heating rate, and temperature tendency due to moist processes. The monthly mean temperature DW1

https://doi.org/10.5194/egusphere-2025-2610
Preprint. Discussion started: 23 June 2025

amplitudes obtained from SABER, MERRA-2 and SD-WACCM-X are calculated. Due to the observational gap of SABER, the Generalized Lomb-Scargle Periodogram is applied to fill the missing data of ozone heating rate. The low-pass filter method is applied to reveal the DW1 QBO variations.

3 Result

3.1 DW1 amplitude response to QBO disruption events

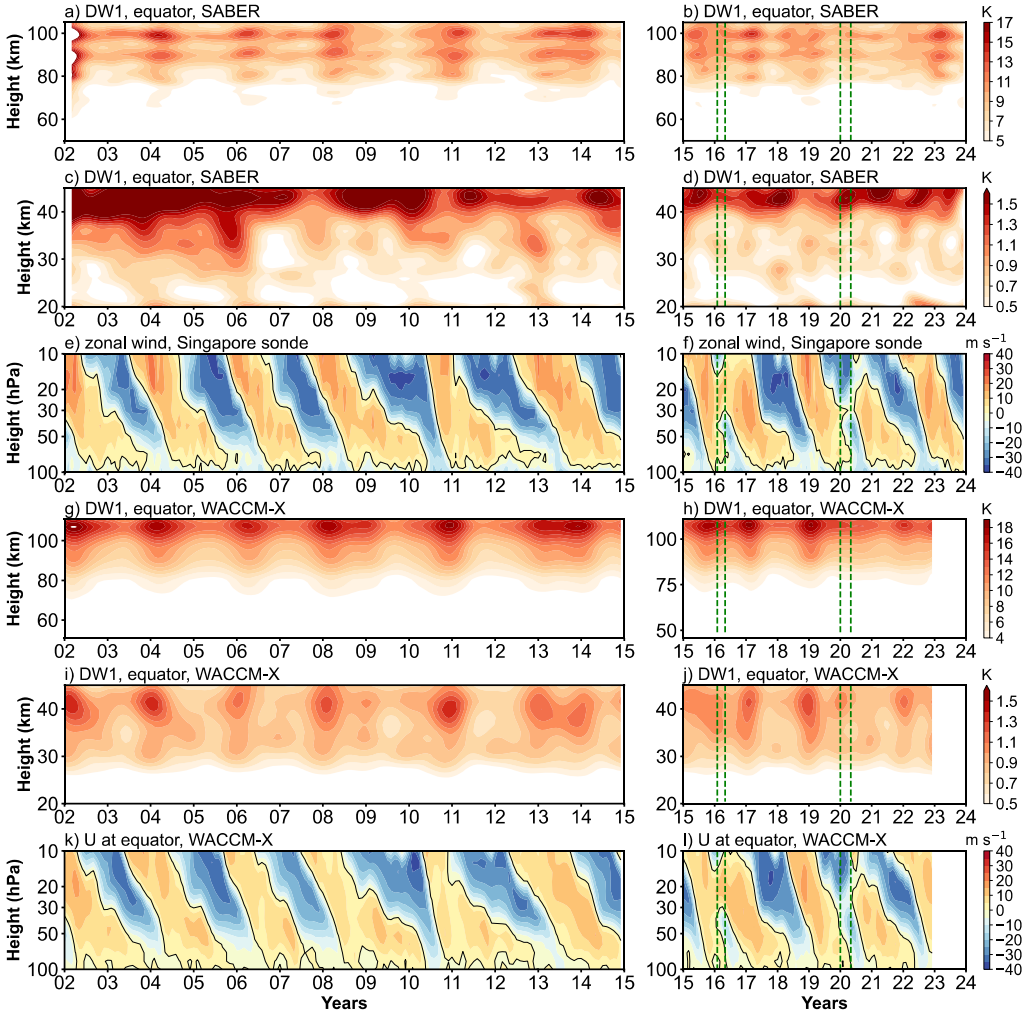

Figure 1. (a, b) Low-pass filtered amplitudes (periods longer than 13 months) of the migrating diurnal tide (DW1; monthly mean, in K) as a function of altitude in the mesosphere and lower thermosphere (MLT) and time (2002–2023), derived from SABER/TIMED temperature observations. (c, d) Same as (a, b) but for the stratosphere. (e, f) Zonal wind at the stratospheric equator from Singapore sonde. (g–i) Similar to (a–f), but based on SD-WACCM-X simulations. Vertical green dashed lines indicate the QBO disruption periods in 2015/16 (February–May 2016) and 2019/20 (January–May 2020).

https://doi.org/10.5194/egusphere-2025-2610
Preprint. Discussion started: 23 June 2025

Figure 1 presents the amplitude of DW1 after low-pass filtering and the zonal wind observed by the Singapore sonde. Only amplitude components longer than 13 months are retained. In the stratosphere, the zonal wind shows alternating downward propagating westerly wind (positive value in Figure 1e and 1f) and easterly wind (negative value in Figure 1e and 1f). Each westerly and easterly transition can be called a QBO cycle. In the stratosphere (Figure 1c and 1d), below 40 km, the amplitude of DW1 also shows Quasi-Biennial variability. Above 40 km, the variation is more complex. This feature will be discussed later. In the MLT region (Figure 1a and 1b), the low-pass filtering results of DW1 at the equator exhibit Quasi-Biennial variability, with amplitude peaks observed around 90 and 100 km. Within each QBO cycle, the DW1 amplitude in the stratosphere below 40 km leads that in the MLT region by one to two months. Comparing the DW1 amplitudes in MLT with the zonal wind, the result reveals that the variations in DW1 amplitude correspond to the zonal wind between 20 and 30 hPa. The amplitude of DW1 is stronger during the QBO westerly wind phase than during the QBO easterly wind phase. This result is consistent with Garcia (2023) that the wind fields of QBO at altitudes below 27 km are clearly correlated with the DW1 amplitude. Accordingly, in this work, the zonal wind between 20 and 30 hPa is used as the criterion for defining the QBO for DW1.

During February–May 2016 and January–May 2020, two QBO disruption events occurred (Wang et al., 2023). As shown in Figure 1f, the phenomenon ranges from 30 to 15 hPa in 2016 and from 40 to 20 hPa in 2020, which is consistent with previous work (Anstey et al., 2021; Newman et al., 2016). Notably, the disruption region coincides with the QBO criterion altitude for DW1. To evaluate how the DW1 exhibits response to the events, the corresponding time intervals are highlighted with vertical green dashed lines. In the stratosphere (Figure 1d), within the disruption periods, amplitude enhancements are observed below 40 km compared to other QBO easterly phases. Similarly, in the MLT region, the DW1 amplitudes show responses to these events (Figure 1b). As shown in Figures 1a and 1b, DW1 amplitudes above 70 km are stronger during these disruption events than during other QBO easterly phases, though they remain weaker than those observed during the QBO westerly phase. This enhancement is particularly evident around 90 and 100 km.

SD-WACCM-X simulations reproduce the SABER observations of DW1 remarkably well in response to QBO disruptions. In Figures 1a, 1b, 1f, and 1g, both datasets show enhanced amplitudes during the February–May 2016 and January–May 2020 events. The difference arises in vertical structure and magnitude. Above 70 km, SABER exhibits three distinct DW1 peaks near 80, 90, and 100 km, whereas SD-WACCM-X shows a single peak at approximately 108 km. In the stratosphere above 40 km, both model and observations peak at similar altitudes, but the simulated amplitudes remain weaker than SABER result. Below 40 km, the model captures the QBO-modulated DW1 seen in Figures 1c, 1d, 1i, and 1j. These discrepancies likely stem from the MERRA-2 nudging applied up to ~50 km in SD-WACCM-X. In this nudged region, DW1 comprises both propagating and non-propagating components (Garcia, 2023; Chapman & Lindzen, 1970). Sakazaki et al. (2018) showed that MERRA-2 may underestimate the contribution of the non-propagation mode of DW1 (Figure 4 in that work). This feature may explain why the amplitude of DW1 is lower than that in SABER and the complex variation of SABER above 40 km.

https://doi.org/10.5194/egusphere-2025-2610
Preprint. Discussion started: 23 June 2025

To assess the DW1 response to QBO disruption events over a broad latitude range, the differences between QBO disruption and regular QBO easterly and westerly are calculated. The DW1 amplitudes used is the result after 13 months low-pass filtering. Since the DW1 amplitudes typically peak between February and April each year (e.g., Xu et al., 2009; Mukhtarov et al., 2009; Garcia, 2023), only the amplitudes during these three months are considered. The classification method for different QBO phases is as follows. Regular QBO phases were classified as following method. QBO westerly phase (QBOW): February–April zonal wind at 20 hPa is continuously westerly, or zonal wind at 30 hPa is westerly while 20 hPa undergoes an easterly-to-westerly transition. Easterly phase (QBOE): any remaining cases. The selection of regular QBO phases is limited to data from 2002 to 2014, as QBO disruption events occurred after 2015. Additionally, since observations in 2002 are mainly available from March to April, data from this year are excluded. The years 2004, 2006, 2008, 2011, 2013, and 2014 are classified as QBOW; 2003, 2005, 2007, 2009, 2010, and 2012 as QBOE. For each phase, all filtered amplitudes across the selected months are averaged, while processing 2016 and 2020 separately. This approach enables a direct comparison of DW1 amplitude anomalies in both latitude and altitude between disruption and regular QBO conditions.

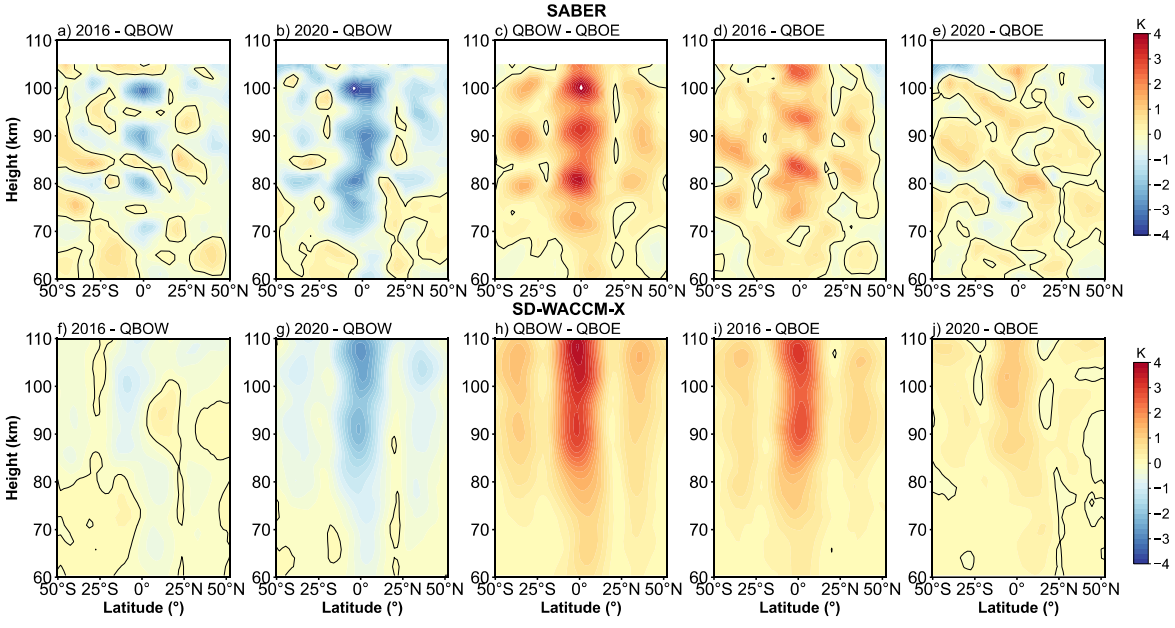

Figure 2. Amplitude differences of the DW1 after low-pass filtering between different QBO phases in the mesosphere and lower thermosphere (MLT) as a function of latitude and altitude. The difference is based on the average from February to April. (a-e) are corresponding to the difference from the 2016 disruption event minus QBO westerly phases (2016-QBOW), 2020 disruption event minus QBO westerly (2020-QBOW), QBO westerly minus QBO easterly (QBOW-QBOE), 2016 disruption event minus QBO easterly (2016-QBOE) and 2020 disruption event minus QBO easterly (2020-QBOE). (f-j) is similar to (a-e) but for SD-WACCM-X simulation result. The black lines indicate the zero lines.

Figure 2 gives the difference in DW1 amplitudes during various QBO phases in the MLT region. The five columns correspond to the 2016 disruption event minus QBO westerly (2016-QBOW), 2020 disruption event minus QBO westerly (2020-QBOW),

https://doi.org/10.5194/egusphere-2025-2610
Preprint. Discussion started: 23 June 2025

QBO westerly minus QBO easterly (QBOW-QBOE), 2016 disruption event minus QBO easterly (2016-QBOE) and 2020 disruption event minus QBO easterly (2020-QBOE), respectively. The relative change between different QBO phases is also calculated (e.g., $\frac{\text{QBOW}-\text{QBOE}}{\text{QBOE}}$, and so on). The comparison between QBOW and QBOE (Figure 2c) reveals that DW1 amplitudes are significantly larger during QBOW, particularly at the equator and around 30°N/S above ~75 km. The enhancements reach ~2.79 K (34.5%) at the equator and ~0.79 K (20.5%) at 30°N/S, with peak values as high as ~3.30 K (38.5%) and ~1.19 K (31.7%) at respective latitudes. During the 2016 disruption (Figures 2a, 2d), DW1 amplitudes lie between QBOE and QBOW values. During the 2016 disruption (Figures 2a, 2d), DW1 amplitudes fall between QBOE and QBOW values. The pattern in 2016–QBOE closely resembles that of QBOW–QBOE, although the equatorial peaks appear at slightly higher altitudes. The peak enhancements relative to QBOE reach ~2.40 K (26.5%) at the equator and ~0.87 K (29.5%) at 30°N/S. Compared to QBOW, however, the equatorial difference drops to –2.28 K (–18.8%). In contrast, the 2020 disruption event shows weaker amplitude increases relative to QBOE (Figures 2b, 2e), with a peak enhancement of only ~0.91 K (11.6%) at the equator and ~0.24 K (11.3%) at 30°N/S. These values are considerably lower than those observed during the 2016 event or the typical QBOW enhancement. The SD-WACCM-X model reproduces the general features described above (Figures 2f–2j), though the vertical structure of the simulated amplitudes differs slightly from observations.

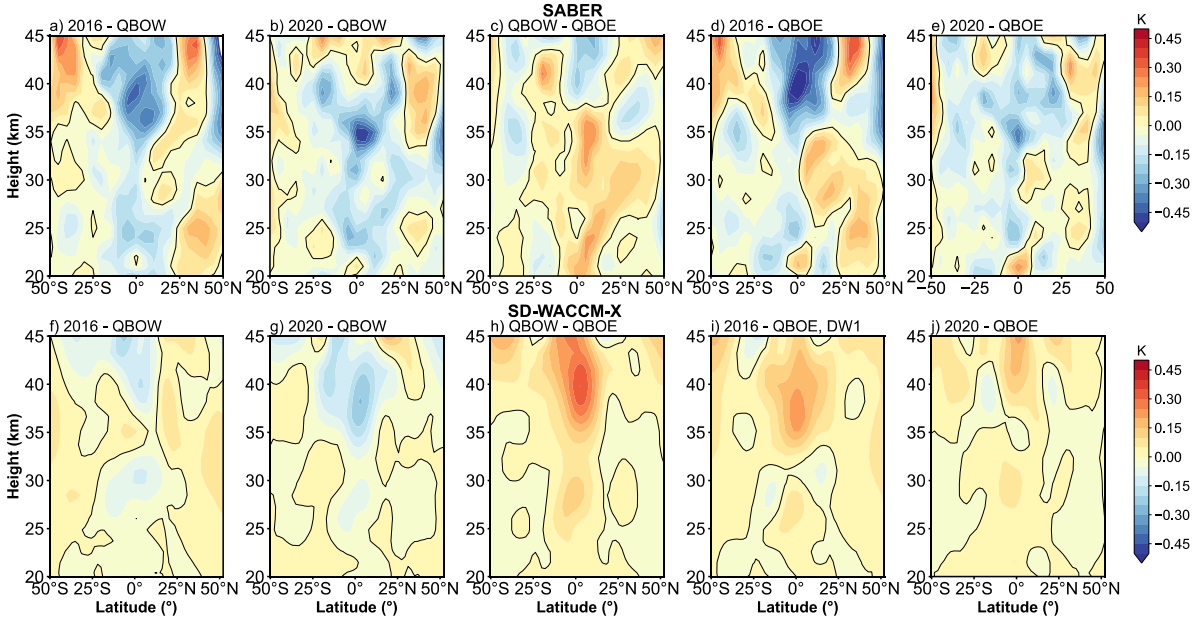

Figure 3. Similar to figure 2 but in stratosphere. (a-e) give the difference result derived from SABER. (f-g) give the difference result derived from SD-WACCM-X.

Figure 3 compares the stratospheric DW1 amplitude differences derived from the SABER dataset and SD-WACCM-X simulations. The enhancement pattern resembles that seen in the MLT region but is confined to tropical latitudes. Because SABER exhibits complex variability above 40 km, the analysis is restricted to altitudes below that level. As shown in Figure

https://doi.org/10.5194/egusphere-2025-2610
Preprint. Discussion started: 23 June 2025

3c, the DW1 amplitudes during QBOW exceed those during the QBOE by ~0.21 K (~37.9 %) at around 20-25 and 30-35 km. In SD-WACCM-X result (Figure 3h), the positive peaks are found at 25-30 km and 35-40 km, which is ~0.21 K (~27.4 %). The amplitudes during the disruption events are much weaker relative to that during QBOW phases shown in both datasets (Figure 3a, 3b, 3f and 3g). Compared to the QBOE, the strengthening during the 2016 QBO disruption event occurs at approximately 30–35 km in SABER (Figure 3d) and 35-45 km in SD-WACCM-X (Figure 3i), which is ~0.15 K (~21.8%) and 0.20 K (~23.9 %), respectively. During the 2020 event, the amplitudes are comparable relative to the QBOE (Figure 3e and 3j).

3.2 DW1 phases response to QBO disruption events

In this section, whether the DW1 phases and wavelengths respond to QBO disruptions will be analysed. As noted previously, the pronounced DW1 amplitude observed from February to April renders the phase during this period an important variable. The mean value and standard deviation derived from the years in different QBO phases (listed in section 3.1) are calculated. The statistical results for the phases in 2016 and 2020 are calculated separately.

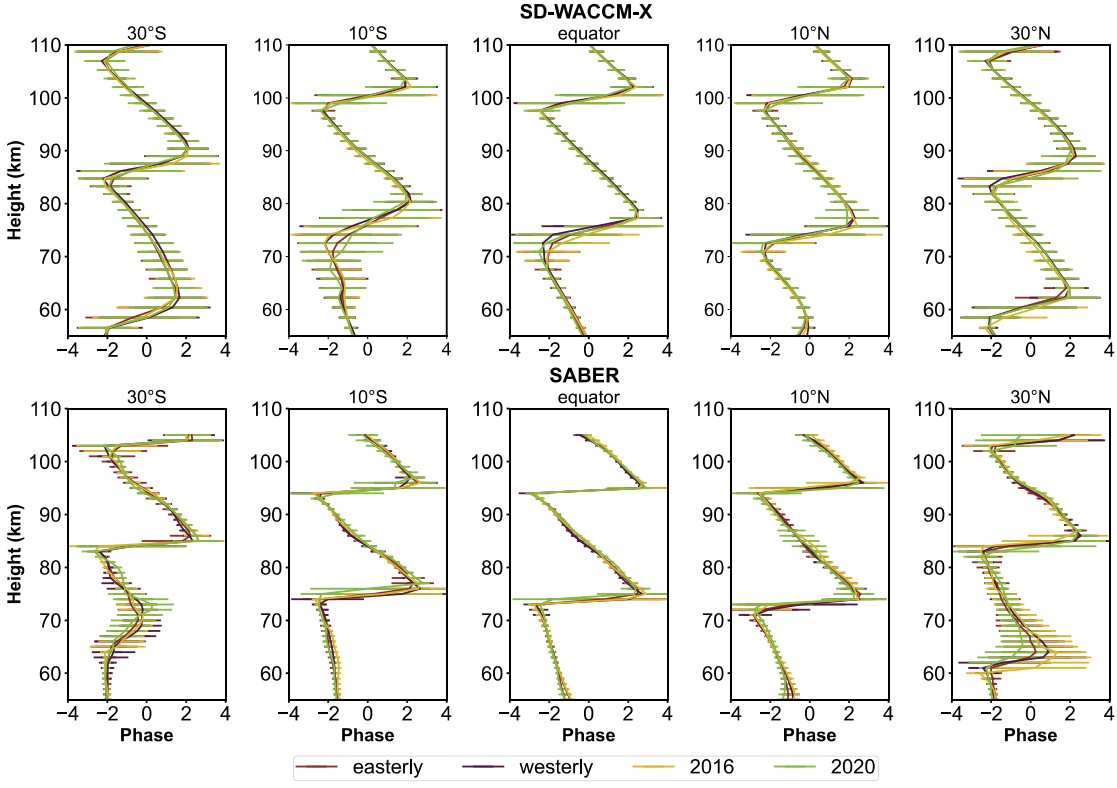

Figure 4. The DW1 vertical phase structure in mesosphere and lower thermosphere (MLT) averaged from February to April during QBO westerly phase (dark red), QBO easterly phase (dark purple), 2016 QBO disruption event (yellow) and 2020 QBO disruption event (green) with respect to SD-WACCM-X (the first row) and SABER (the second row). The latitude covers 30°S, 10°S, 0°, 10°N, 30°N. The error bar denotes one standard deviation of the phases for each height.

https://doi.org/10.5194/egusphere-2025-2610
Preprint. Discussion started: 23 June 2025

Figures 4 and 5 illustrate the vertical phase structure of DW1 in the mesosphere and lower thermosphere (MLT) and stratospheric regions, respectively, averaged over the February–April period. The results are presented for various QBO phases at different latitudes, based on data from SD-WACCM-X (top row) and SABER (bottom row). Error bars indicate one standard deviation of the phase values. The lines represent different QBO phases and events: QBO westerly phase (dark red), QBO easterly phase (dark purple), the 2016 QBO disruption event (yellow), and the 2020 QBO disruption event (green). Latitudes with large amplitudes are selected, which are 30°N/S, 10°N/S and the equator.

In the MLT region (Figure 4), the vertical phase profiles exhibit minimal differences across the four QBO phases. The structures are nearly identical in both the simulations and observations, with two phase peaks (approximately π rad) consistently present. At each latitude, the peak altitudes remain almost unchanged among the different QBO phases, suggesting a limited phase response to QBO disruption events in the MLT region.

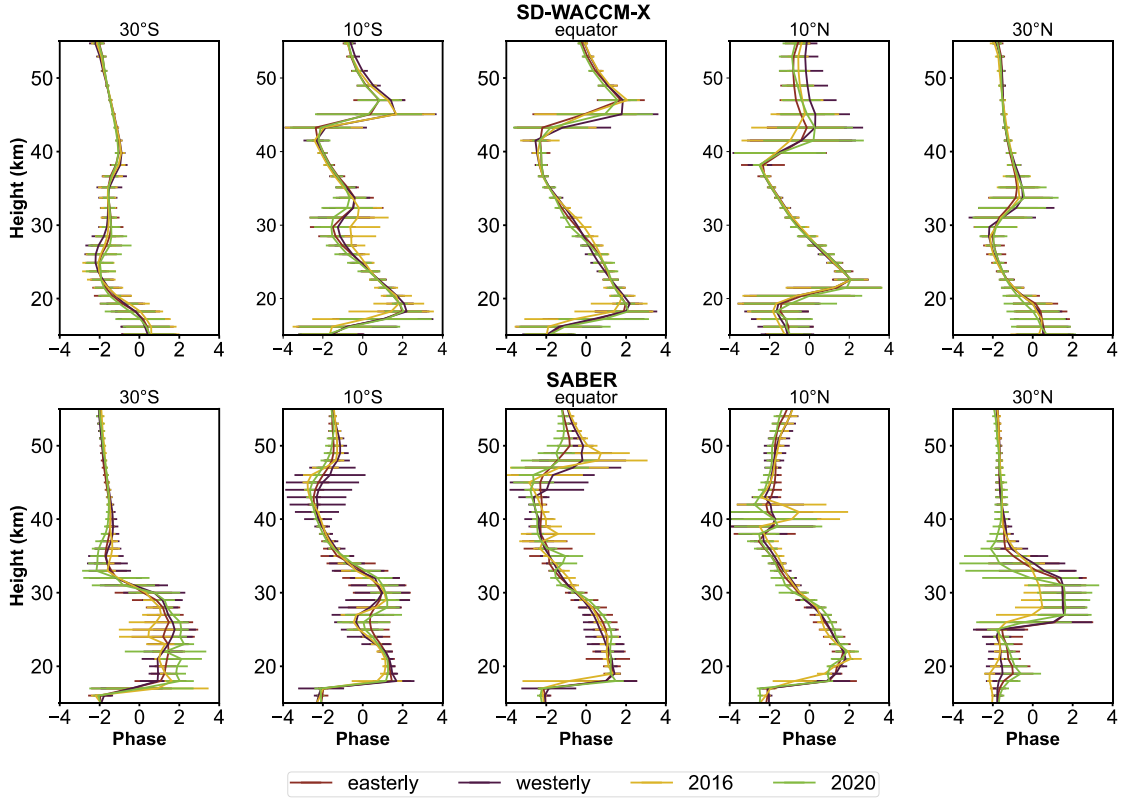

Figure 5. Similar to Figure 2 but in stratosphere. The first row gives the result derived from SD-WACCM-X. The second row gives the result derived from SABER.

The DW1 vertical phase structures in the stratosphere region are given in Figure 5. Similarly, the structure and phase peak altitudes around the tropics and at 30°N/S show little variation among the four QBO phases revealed by both datasets. In the

https://doi.org/10.5194/egusphere-2025-2610
Preprint. Discussion started: 23 June 2025

tropical region of SABER dataset, the phase structure is different from the result shown in SD-WACCM-X between various QBO phases at around 40-50 km. As introduced above, the SD-WACCM-X dataset may underestimate the influence of non-propagation mode due to the nudging of MERRA-2. The effect of the non-propagating mode then results in the phase difference in these two datasets (See Figure 4b of Sakazaki et al., 2017).

The phase peaks described above (~π rad) are used to calculate the DW1 wavelengths in both the stratosphere and MLT regions. The altitude difference between the two peaks is taken as the wavelength, following Liu et al. (2021). The wavelength is not considered at 30°N/S in the stratosphere because the non-propagating mode dominates this region. The statistical results of DW1 wavelengths under different QBO phases are summarized in Table 1, which lists the mean values and standard deviations at various latitudes. In the MLT region, the mean wavelengths are ~20 km in the SABER dataset and ~25 km in the SD-WACCM-X dataset. The wavelengths during QBO disruption events are comparable to those during the QBO westerly and easterly phases, a feature also captured in the SD-WACCM-X simulations. In the stratosphere, the mean wavelengths are ~27 km in SD-WACCM-X and ~30 km in SABER. At the equator, only minor differences are observed among the four QBO phases, which is consistent with the vertical structures shown in Figures 4 and 5.

Table 1. The comparison of mean (left of the slash) and standard deviations (right of the slash) of DW1 wavelengths (in km) revealed by SD-WACCM-X and SABER in MLT and stratosphere (Stra) between QBO westerly phase, easterly phase, 2016 disruption event and 2020 disruption event calculated from February to April.

Data	SD-WACCM-X				SABER			
latitude	30°S	0°		30°N	30°S	0°		30°N
		MLT	Stra			MLT	Stra	
Westerly	27.96 /3.67	24.52 /1.94	26.92 /1.69	25.03 /2.38	19.36 /1.42	20.95 /0.47	29.17 /2.25	19.63 /2.20
Easterly	26.85 /3.75	25.01 /2.52	27.98 /2.05	24.49 /2.84	19.04 /1.32	20.52 /0.63	31.03 /3.32	19.42 /1.45
2016	26.53 /3.95	25.48 /2.61	27.00 /2.26	25.48 /2.76	19.04 /0.62	20.86 /0.35	29.32 /1.69	19.31 /1.57
2020	26.81 /3.85	24.76 /1.93	27.58 /2.43	24.69 /2.55	19.43 /1.39	19.77 /1.02	31.76 /2.96	18.45 /1.62

https://doi.org/10.5194/egusphere-2025-2610
Preprint. Discussion started: 23 June 2025

4 Discussion

The influence of QBO disruption events on DW1 can be traced back to its excitation mechanisms. The excitation sources of DW1 can be broadly classified into three categories: (1) solar radiation in the near-infrared (IR) absorbed by tropospheric H_2O, (2) solar radiation in the ultraviolet (UV) absorbed by stratospheric and lower mesospheric O_3, and (3) solar radiation absorbed by O_2 in the Schumann–Runge bands and continuum (Hagan, 1996). Water vapor and ozone are closely associated with QBO variations. Additionally, Kogure and Liu (2021) suggested the role of latent heating in modulating DW1. It is worth noting that the timing of the 2016 QBO disruption event coincides with the phase of the extreme El Niño (e.g., Santoso et al., 2017; Hu and Fedorov, 2017). So, the contribution of latent heating should be paid attention.

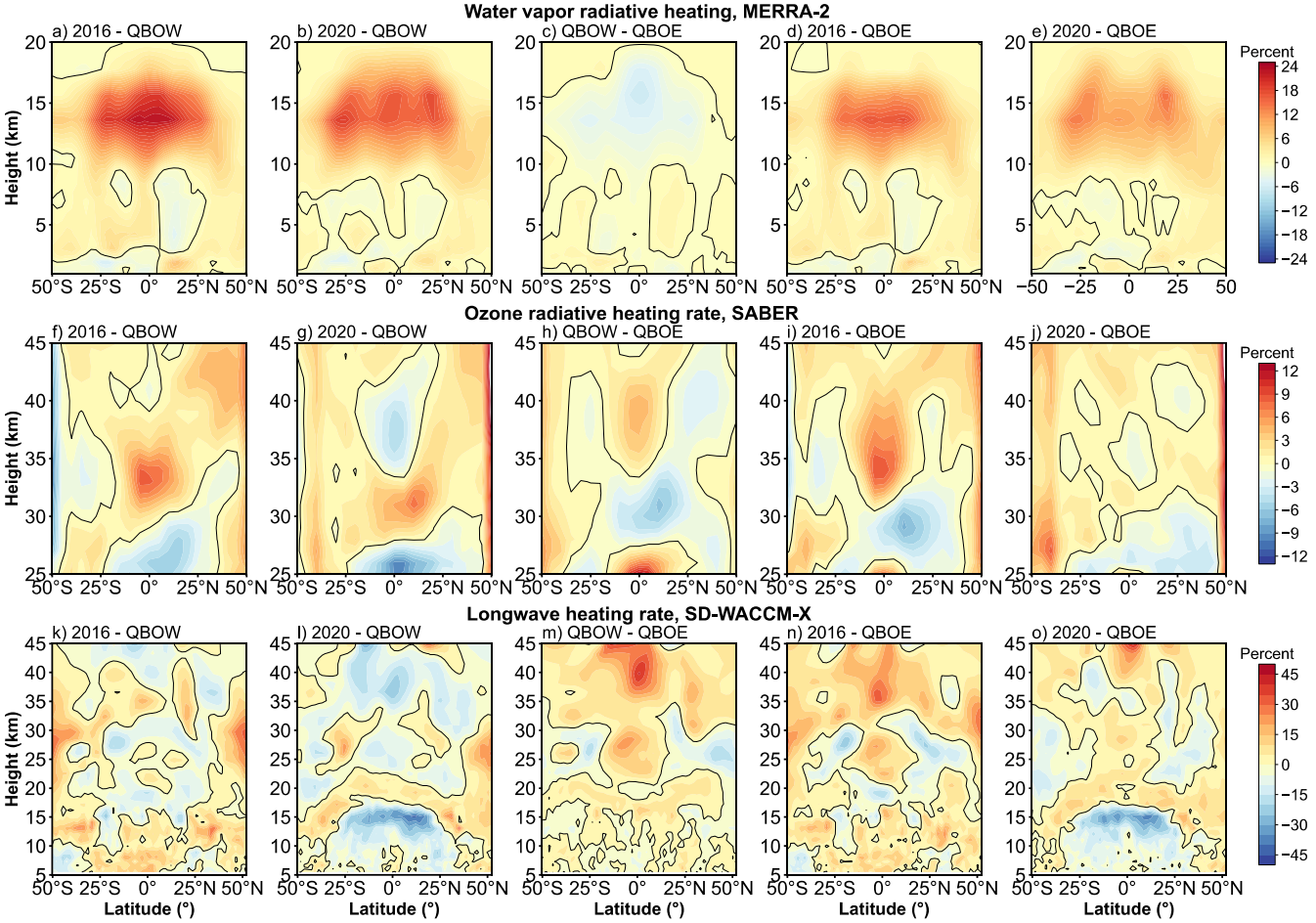

Figure 6. As in Figure 2 and Figure 3, but the relative changes of amplitude (in percent) in DW1 component (after low-filtering) of (a-e) water vapor heating rate DW1 component from MERRA-2, (f-j) ozone heating rate DW1 component from SABER and (k-o) longwave heating rate from SD-WACCM-X.

https://doi.org/10.5194/egusphere-2025-2610
Preprint. Discussion started: 23 June 2025

Given the strong vertical gradients in radiative heating rates, Figure 6 presents the relative changes in the DW1 component of water vapor radiative heating rate, ozone radiative heating rate, and longwave heating rate. The calculation method is consistent with the method given in Section 3.1. During QBOE and QBOW, the DW1 component of water vapor heating remains nearly unchanged (Figure 6c). However, during the 2016 QBO disruption (Figures 6a, 6d), a notable enhancement in water vapor heating appears between 10–18 km altitude across 30°S–30°N, with increases of ~14% relative to QBOW and ~10% relative to QBOE. A similar pattern is seen during the 2020 QBO disruption event (Figures 6b and 6e), with three positive peaks appearing near 25°S, 25°N and equator. The relative changes of regional average rise by ~12 % compared to QBOW and ~9 % compared to QBOE, with peak anomalies of ~16 % and ~11 %, respectively. These enhancements suggest that water vapor radiative heating may contribute to the strengthening of DW1 amplitudes during QBO disruption events. Nevertheless, it is important to consider the vertical distribution of heating: while the water vapor heating rate near the tropical tropopause is only ~0.014 K day^{-1}, the primary heating maximum near 8.4 km reaches ~1.05 K day^{-1}. As such, further investigation is needed to quantify the extent to which relatively weak heating at tropopause levels can influence DW1 excitation.

Xu et al. (2010) found that, due to ozone's long chemical lifetime, it does not exhibit significant diurnal variation. Wang et al. (2024) suggested that ozone concentration during QBO disruption events is modulated. Therefore, the variation of the ozone concentration during the disruption events and the diurnal variation of solar radiation could modulate ozone radiative heating, which in turn may influence the changes of DW1 amplitudes. Figures 6f–6j reveal that the largest QBO-related differences in the DW1 component of ozone heating occur near the equator between 30 and 45 km. In QBOW, ozone heating rates between 35 and 45 km exceed those in QBOE by ~3.6 % (Figure 6h). During the 2016 QBO disruption event (Figures 6f and 6i), ozone radiative heating rates are ~6.1 % larger than those in the QBOW between 30 and 35 km and ~6.6 % larger than those in the QBOE within the 30–40 km range. In contrast, during the 2020 disruption event (Figures 6g and 6j), the ozone heating rate is comparable to that of the easterly phase and lower than that of the westerly phase in the 35–45 km altitude range. In summary, the pronounced increase in ozone radiative heating during the 2016 disruption likely contributes to the observed amplification of DW1 amplitudes, whereas the much smaller ozone response in 2020 suggests a correspondingly weaker influence on the DW1 amplitudes.

In the SD-WACCM-X simulation, the longwave heating rate accounts for the effects of three major absorbers: H_2O, CO_2, and O_3 (Neale et al., 2010). This parameter could be used to verify the effect of the water vapor and ozone radiative heating. The DW1 component of the longwave heating rate from SD-WACCM-X is shown in Figures 6k–6o. The heating rate difference between the QBOW and QBOE reveals a positive peak at 40 km near the equator, with no significant difference at the equatorial tropopause (Figure 6m). The feature corresponds to the observed pattern (Figures 6c and 6h). In the 2016 disruption case, the simulated equatorial heating rate exhibits positive peaks around 35 km and 15 km (Figure 6k and 6n), aligning well with observations in terms of altitude, though discrepancies remain in the latitudinal distribution (Figures 6a, 6f, 6d, and 6i). In the 2020 disruption case, the simulation (Figure 6l and 6o) agrees with the observed stratospheric heating features (Figures 6g and 6j). However, at around 15 km, the simulation shows negative peaks near the tropopause, whereas the observations indicate positive peaks (Figures 6b and 6e). As longwave heating incorporates contributions from multiple absorbers, the

https://doi.org/10.5194/egusphere-2025-2610
Preprint. Discussion started: 23 June 2025

discrepancies may be attributed to the influence of other constituents. Overall, both simulations and observations suggest that water vapor and ozone radiative heating may play critical roles in modulating DW1.

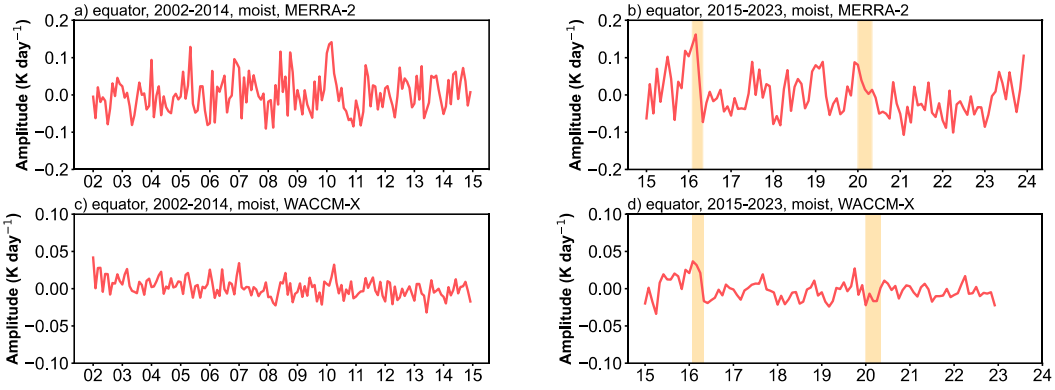

Figure 7. (a, b) The deseasonalized time series of DW1 amplitudes of latent heating rate (K day^{-1}) at equator averaged from 800 hPa to 200 hPa derived from MERRA-2. (c-d) is as in (a-b) but from SD-WACCM-X. The orange-filled areas represent two QBO disruption events.

Figure 7 shows the deseasonalized time series of the DW1 component of latent heating rate (K day^{-1}) at the equator, averaged from 800 hPa to 200 hPa. In this tropospheric layer, the latent-heating signal shows less differences between QBOW and QBOE phases. Therefore, deseasonalization is directly applied to the full time series without separating the two QBO states. In MERRA-2 and SD-WACCM-X, the anomaly peaks reach 0.162 K day^{-1} and 0.037 K day^{-1}, respectively, which correspond to increases of about 32 % and 25 % above their climatological means (0.50 K day^{-1} and 0.15 K day^{-1}). When averaged over the February-April in 2016, the anomalies remain elevated at 0.11 K day^{-1} (22.0 %) in MERRA-2 and 0.03 K day^{-1} (19.2 %) in SD-WACCM-X. In contrast, during the 2020 QBO disruption event, the amplitudes in both MERRA-2 and SD-WACCM-X remain closer to the climatological means, with deviations of 0.018 K day^{-1} and -0.013 K day^{-1}, respectively. These results suggest that latent heating may contribute to the amplification of DW1 amplitudes during the 2016 QBO disruption event but show little effect during the 2020 event.

Based on the discussion above, the enhancement of water vapor radiative heating, ozone radiative heating and latent heating during the 2016 disruption event may contribute to the amplified DW1 amplitudes observed during that period. In contrast, during the 2020 disruption event, the enhancement of water vapor radiative heating likely impacts the modest DW1 amplitude enhancement. However, there still requires quantifying the fractional contribution of each heat source to the total DW1 amplitude and assessing how the tropically confined ozone heating projects onto low-latitude tidal modes. These issues is worth investigating in future work.

https://doi.org/10.5194/egusphere-2025-2610
Preprint. Discussion started: 23 June 2025

5 Summary

In this work, the response of global DW1 amplitudes and phases during QBO disruption events is investigated using SABER observation, MERRA-2 dataset and SD-WACCM-X simulation results from 2002 to 2023. Additionally, the variation of excitation sources during the event is explored. The findings are summarized as follows:

(1) The DW1 vertical phase structure and wavelengths show less response to these two QBO disruption events. Few differences are observed in the phase structures and wavelengths between the disruption periods and the typical QBO westerly and easterly phases.

(2) In the 2016 QBO disruption event, DW1 amplitudes are markedly enhanced relative to regular QBO easterly (QBOE) conditions. In the mesosphere and lower thermosphere (MLT), the mean enhancement reaches ~2.79 K (34.5 %) at the equator and ~0.79 K (20.5 %) at 30° N/S, with peaks of ~3.30 K (38.5 %) and ~1.19 K (31.7 %) at the same latitudes. A pronounced increase is also evident in the stratosphere near the equator (~0.15 K, ~21.8%). By contrast, the 2020 disruption shows only a modest rise in DW1 amplitude relative to the regular QBOE. In the MLT, peak anomalies reach ~0.91 K (11.6 %) at the equator and ~0.24 K (11.3 %) at 30° N/S, whereas in the stratosphere the DW1 amplitude remains virtually unchanged.

(3) During the 2016 event, water vapour radiative heating, ozone radiative heating and latent heating increase by ~10 %, ~6.6 % and ~22 % relative to QBOE. During the 2020 event, only water vapour radiative heating exhibits a clear rise (~9 %), whereas the ozone heating and latent heating is close to the QBOE. The amplification of water vapour, ozone, and latent heating could account for the significant DW1 amplitude increase in 2016 event, while the enhancement of water vapour heating may explain the weaker response in 2020 event.

This work analyses the feature how the DW1 varies when the highly unusual wind of QBO occurs. This phenomenon which is found in responses at different atmospheric layers suggests an atmosphere coupling process. The observations and model simulations give clear evidence of the connection. The possible link between the lower atmosphere trace gases variation and MLT dynamic features is shown during these unique events. The result gives a window for exploring the mechanism of the coupling, providing a basis for future research on the underlying mechanisms.

Appendix A: approach for calculating the water vapor radiative heating rate

The heating rate for water vapor mainly follows the method from Groves et al. (1982) and Lieberman et al. (2003). As mentioned in equation 1, the heating rate could be categorized into clear sky and cloudy sky. The equation of clear sky is given by Lacis and Hansen (1974):

$$J_{clr} = q\eta^c S_0 \cos\zeta \left[MA(y) + \frac{5}{3} RA(y')\right] \quad (A1)$$

with q is water vapor mixing ratio (specific humidity), η is defined as p/p$_0$, c is defined as $0.75 - \Gamma R_M/2g$. Γ is the vertical lapse rate, which is 6.5K km^{-1}. R_M is the gas constant for air. g is the acceleration of gravity. S_0 is the solar constant, which is 1353 W m^{-2}. ζ is the solar zenith angle, the equation is:

https://doi.org/10.5194/egusphere-2025-2610
Preprint. Discussion started: 23 June 2025

$$\cos\zeta = \sin\theta\,\sin\delta + \cos\theta\,\cos\delta\,\cos t' \tag{A2}$$

with θ is the latitude, δ is the solar declination. t' is given by following equation:

$$t' = \lambda + \Omega t \tag{A3}$$

with λ is longitude in radiance, Ω is the angular frequency of Earth's rotation. t is the universal time.

M is given by equation:

$$M = \frac{35}{(1224\cos^2\zeta + 1)^{\frac{1}{2}}} \tag{A4}$$

A(y) is given by equation:

$$A(y) = 2.9\left[\frac{0.635 + 0.365Y}{(Y^{0.635} + 5.925y)^2 Y^{0.365}}\right]\mathrm{cm^2 g^{-1}} \tag{A5}$$

with:

$$Y = 1 + 141.5y \tag{A6}$$

and

$$y = M\bar{w} \tag{A7}$$

and

$$y' = M\bar{w}_t + \frac{5}{3}(\bar{w}_t - \bar{w}) \tag{A8}$$

The $\bar{w}$ is the effective water vapor amount, is given by equation:

$$\bar{w} = \int_z^\infty q\rho(p/p_0)^{.75}(T_0/T)^{1/2}dz \tag{A9}$$

Where ρ is the air density. $\bar{w}_t$ is the total water vapor above the reflecting surface.

The cloudy sky heating rate is given by Groves (1982):

$$J_{cld} = q\eta^c S_0 \cos\zeta Z \tag{A10}$$

with Z is parameter given by:

$$Z = \sum_i \{ak'[\cosh(\xi_0 + \beta - \xi)) - \cosh(\xi_0 + \beta' - \xi)]/\sinh(\xi_0 + \beta)\}_i \tag{A11}$$

with ξ is given by:

$$\xi = k'\bar{w} \tag{A12}$$

$$k' = \frac{5}{3}\alpha(\sigma + k) \tag{A13}$$

with α, β and β':

$$\alpha = (1-\omega)^{\frac{1}{2}}(1 + \omega - 2\omega f)^{\frac{1}{2}} \tag{A14}$$

https://doi.org/10.5194/egusphere-2025-2610
Preprint. Discussion started: 23 June 2025

$$\beta = \frac{1}{2}\ln\{[1+\alpha-\omega f-R\omega(1-f)]\div[1-\alpha-\omega f-R\omega(1-f)]\} \quad (A15)$$

$$\beta' = \beta + \frac{1}{2}\ln\left[\frac{1-\alpha-\omega f}{1+\alpha-\omega f}\right] \quad (A16)$$

with single scattering albedo:

$$\omega = \frac{\sigma}{\sigma + k} \quad (A17)$$

where σ = 40 cm^{-1}, f is 0.925, k and a are given by table 2 from Somerville et al. (1974).

Data availability. SABER data is available from the SABER project data server at https://spdf.gsfc.nasa.gov/pub/data/timed/saber/. The QBO index is retrieved from https://acd-ext.gsfc.nasa.gov/Data_services/met/qbo/QBO_Singapore_Uvals_GSFC.txt. The Generalized Lomb-Scargle Periodogram and best-frequency fit method are provided by PyAstronomy (https://github.com/sczesla/PyAstronomy). The MERRA-2 reanalysis data can be retrieved from https://disc.gsfc.nasa.gov/datasets/M2T3NVASM_5.12.4/summary/ (zonal wind, temperature, cloud fraction, specific humidity), https://disc.gsfc.nasa.gov/datasets/M2I3NVAER_5.12.4/summary (air density), https://disc.gsfc.nasa.gov/datasets/M2T1NXRAD_5.12.4/summary (surface albedo), https://disc.gsfc.nasa.gov/datasets/M2T3NPTDT_5.12.4/summary?keywords=MERRA2%20tdt (tendency of air temperature due to moist processes).

Author contributions. Conceptualization: SL, GYJ; investigation: SL; methodology: SL, GYJ; project administration: BXL, GYJ and YJZ; software: SL; supervision: GYJ, BXL and YJZ; validation: BXL, GYJ and YJZ; visualization: SL; writing – original draft preparation: SL; and writing – review and editing: GYJ, BXL, XL, JYX, YJZ and WY. All authors have read and agreed to the published version of the paper.

Competing interests. The authors declare that they have no conflict of interest.

Disclaimer. Publisher's note: Copernicus Publications remains neutral with regard to jurisdictional claims made in the text, published maps, institutional affiliations, or any other geographical representation in this paper. While Copernicus Publications makes every effort to include appropriate place names, the final responsibility lies with the authors.

Acknowledgements. WACCM-X SD output data have been used in this study, and we would like to acknowledge the WACCM-X development group at NCAR/HAO for making the model output publicly available. This work was jointly

supported by the Strategic Priority Research Program of the Chinese Academy of Sciences (Grant No. XDB0560000), the Pandeng Program of National Space Science Center CAS, National Key R&D program of China (2023YFB3905100), the Project of Stable Support for Youth Team in Basic Research Field, CAS (YSBR-018), the National Natural Science Foundation of China (42174212), the Chinese Meridian Project, and the Specialized Research Fund for State Key Laboratories.

Financial support. This work was jointly supported by the Strategic Priority Research Program of the Chinese Academy of Sciences (Grant No. XDB0560000), the Pandeng Program of National Space Science Center CAS, National Key R&D program of China (2023YFB3905100), the Project of Stable Support for Youth Team in Basic Research Field, CAS (YSBR-018), the National Natural Science Foundation of China (42174212), the Chinese Meridian Project, and the Specialized Research Fund for State Key Laboratories.

References

Anstey, J. A., Banyard, T. P., Butchart, N., Coy, L., Newman, P. A., Osprey, S., and Wright, C. J.: Prospect of Increased Disruption to the QBO in a Changing Climate, Geophys. Res. Lett., 48, 10.1029/2021gl093058, 2021.

Baldwin, M. P., Gray, L. J., Dunkerton, T. J., Hamilton, K., Haynes, P. H., Randel, W. J., Holton, J. R., Alexander, M. J., Hirota, I., Horinouchi, T., Jones, D. B. A., Kinnersley, J. S., Marquardt, C., Sato, K., and Takahashi, M.: The quasi-biennial oscillation, Rev. Geophys., 39, 179-229, 10.1029/1999rg000073, 2001.

Cen, Y., Yang, C., Li, T., Russell Iii, J. M., and Dou, X.: Suppressed migrating diurnal tides in the mesosphere and lower thermosphere region during El Niño in northern winter and its possible mechanism, Atmos. Chem. Phys., 22, 7861-7874, 10.5194/acp-22-7861-2022, 2022.

Chapman, S. and Lindzen, R.: Atmospheric tides – thermal and gravitational, D. Reidel Publishing Company, Dordrecht, the Netherlands, ISBN 978-94-010-3401-2, 1970.

Davis, R. N., Du, J., Smith, A. K., Ward, W. E., and Mitchell, N. J.: The diurnal and semidiurnal tides over Ascension Island (° S, 14° W) and their interaction with the stratospheric quasi-biennial oscillation: studies with meteor radar, eCMAM and WACCM, Atmos. Chem. Phys., 13, 9543-9564, 10.5194/acp-13-9543-2013, 2013.

de Araújo, L. R., Lima, L. M., Jacobi, C., and Batista, P. P.: Quasi-biennial oscillation signatures in the diurnal tidal winds over Cachoeira Paulista, Brazil, J. Atmos. Sol. Terr. Phys., 155, 71-78, 10.1016/j.jastp.2017.02.001, 2017.

Dhadly, M. S., Emmert, J. T., Drob, D. P., McCormack, J. P., and Niciejewski, R. J.: Short-Term and Interannual Variations of Migrating Diurnal and Semidiurnal Tides in the Mesosphere and Lower Thermosphere, J. Geophys. Res.: Space Phys., 123, 7106-7123, 10.1029/2018ja025748, 2018.

https://doi.org/10.5194/egusphere-2025-2610
Preprint. Discussion started: 23 June 2025

Diallo, M., Riese, M., Birner, T., Konopka, P., Müller, R., Hegglin, M. I., Santee, M. L., Baldwin, M., Legras, B., and Ploeger, F.: Response of stratospheric water vapor and ozone to the unusual timing of El Niño and the QBO disruption in 2015–2016, Atmos. Chem. Phys., 18, 13055-13073, 10.5194/acp-18-13055-2018, 2018.

Diallo, M. A., Ploeger, F., Hegglin, M. I., Ern, M., Grooß, J.-U., Khaykin, S., and Riese, M.: Stratospheric water vapour and ozone response to the quasi-biennial oscillation disruptions in 2016 and 2020, Atmos. Chem. Phys., 22, 14303-14321, 10.5194/acp-22-14303-2022, 2022.

Ern, M., Ploeger, F., Preusse, P., Gille, J. C., Gray, L. J., Kalisch, S., Mlynczak, M. G., Russell, J. M., and Riese, M.: Interaction of gravity waves with the QBO: A satellite perspective, J. Geophys. Res.: Atmos., 119, 2329-2355, 10.1002/2013jd020731, 2014.

Gan, Q., Du, J., Ward, W. E., Beagley, S. R., Fomichev, V. I., and Zhang, S.: Climatology of the diurnal tides from eCMAM30 (1979 to 2010) and its comparison with SABER, Earth Planets Space, 66, 10.1186/1880-5981-66-103, 2014.

Garcia, R. R.: On the Structure and Variability of the Migrating Diurnal Temperature Tide Observed by SABER, J. Atmos. Sci., 80, 687-704, 10.1175/jas-d-22-0167.1, 2023.

Garcia, R. R., Marsh, D. R., Kinnison, D. E., Boville, B. A., and Sassi, F.: Simulation of secular trends in the middle atmosphere, 1950–2003, J. Geophys. Res.: Atmos., 112, 10.1029/2006jd007485, 2007.

Gelaro, R., McCarty, W., Suarez, M. J., Todling, R., Molod, A., Takacs, L., Randles, C., Darmenov, A., Bosilovich, M. G., Reichle, R., Wargan, K., Coy, L., Cullather, R., Draper, C., Akella, S., Buchard, V., Conaty, A., da Silva, A., Gu, W., Kim, G. K., Koster, R., Lucchesi, R., Merkova, D., Nielsen, J. E., Partyka, G., Pawson, S., Putman, W., Rienecker, M., Schubert, S. D., Sienkiewicz, M., and Zhao, B.: The Modern-Era Retrospective Analysis for Research and Applications, Version 2 (MERRA-2), J Clim, Volume 30, 5419-5454, 10.1175/JCLI-D-16-0758.1, 2017.

Groves, G. V.: Hough components of water vapour heating, J. Atmos. Terr. Phys., 44, 281-290, 10.1016/0021-9169(82)90033-2, 1982.

Hagan, M. E.: Comparative effects of migrating solar sources on tidal signatures in the middle and upper atmosphere, J. Geophys. Res.: Atmos., 101, 21213-21222, 10.1029/96jd01374, 1996.

Hagan, M. E., Burrage, M. D., Forbes, J. M., Hackney, J., Randel, W. J., and Zhang, X.: QBO effects on the diurnal tide in the upper atmosphere, Earth Planets Space, 51, 571-578, 10.1186/BF03353216, 1999.

Holton, J. R. and Lindzen, R. S.: An Updated Theory for the Quasi-Biennial Cycle of the Tropical Stratosphere, J. Atmos. Sci., 29, 1076-1080, 10.1175/1520-0469(1972)029<1076:Autftq>2.0.Co;2, 1972.

Hu, S. and Fedorov, A. V.: The extreme El Niño of 2015–2016 and the end of global warming hiatus, Geophys. Res. Lett., 44, 3816-3824, 10.1002/2017gl072908, 2017.

Jiang, G., Xu, J., Shi, J., Yang, G., Wang, X., and Yan, C.: The first observation of the atmospheric tides in the mesosphere and lower thermosphere over Hainan, China, Chin. Sci. Bull., 55, 1059-1066, 10.1007/s11434-010-0084-8, 2010.

Kang, M.-J. and Chun, H.-Y.: Contributions of equatorial waves and small-scale convective gravity waves to the 2019/20 quasi-biennial oscillation (QBO) disruption, Atmos. Chem. Phys., 21, 9839-9857, 10.5194/acp-21-9839-2021, 2021.

https://doi.org/10.5194/egusphere-2025-2610
Preprint. Discussion started: 23 June 2025

Kang, M.-J., Chun, H.-Y., Son, S.-W., Garcia, R. R., An, S.-I., and Park, S.-H.: Role of tropical lower stratosphere winds in quasi-biennial oscillation disruptions, Sci. Adv., 8, 10.1126/sciadv.abm7229, 2022.

Kogure, M. and Liu, H.: DW1 Tidal Enhancements in the Equatorial MLT During 2015 El Niño: The Relative Role of Tidal Heating and Propagation, J. Geophys. Res.: Space Phys., 126, 10.1029/2021ja029342, 2021.

Lacis, A. A. and Hansen, J.: A Parameterization for the Absorption of Solar Radiation in the Earth's Atmosphere, J. Atmos. Sci., 31, 118-133, 10.1175/1520-0469(1974)031<0118:Apftao>2.0.Co;2, 1974.

Lieberman, R. S., Ortland, D. A., and Yarosh, E. S.: Climatology and interannual variability of diurnal water vapor heating, J. Geophys. Res.: Atmos., 108, 10.1029/2002jd002308, 2003.

Lieberman, R. S., Riggin, D. M., Ortland, D. A., Nesbitt, S. W., and Vincent, R. A.: Variability of mesospheric diurnal tides and tropospheric diurnal heating during 1997–1998, J. Geophys. Res., 112, 10.1029/2007jd008578, 2007.

Lindzen, R. S. and Holton, J. R.: A Theory of the Quasi-Biennial Oscillation, J. Atmos. Sci., 25, 1095-1107, 10.1175/1520-0469(1968)025<1095:Atotqb>2.0.Co;2, 1968.

Liu, G., Lieberman, R. S., Harvey, V. L., Pedatella, N. M., Oberheide, J., Hibbins, R. E., Espy, P. J., and Janches, D.: Tidal Variations in the Mesosphere and Lower Thermosphere Before, During, and After the 2009 Sudden Stratospheric Warming, J. Geophys. Res.: Space Phys., 126, 10.1029/2020ja028827, 2021.

Liu, S., Jiang, G., Luo, B., Xu, J., Lin, R., Zhu, Y., and Liu, W.: Solar Cycle Dependence of Migrating Diurnal Tide in the Equatorial Mesosphere and Lower Thermosphere, Remote Sens., 16, 10.3390/rs16183437, 2024a.

Liu, Y., Xu, J., Smith, A. K., and Liu, X.: Seasonal and Interannual Variations of Global Tides in the Mesosphere and Lower Thermosphere Neutral Winds: I. Diurnal Tides, J. Geophys. Res.: Space Phys., 129, 10.1029/2023ja031887, 2024b.

Marsh, D. R., Mills, M. J., Kinnison, D. E., Lamarque, J.-F., Calvo, N., and Polvani, L. M.: Climate Change from 1850 to 2005 Simulated in CESM1(WACCM), J. Clim., 26, 7372-7391, 10.1175/jcli-d-12-00558.1, 2013.

Mayr, H. G., Mengel, J. G., Talaat, E. R., Porter, H. S., and Chan, K. L.: Mesospheric non-migrating tides generated with planetary waves: I. Characteristics, J. Atmos. Sol. Terr. Phys., 67, 959-980, 10.1016/j.jastp.2005.03.002, 2005.

Mertens, C. J.: SABER observations of mesospheric temperatures and comparisons with falling sphere measurements taken during the 2002 summer MaCWAVE campaign, Geophys. Res. Lett., 31, 10.1029/2003gl018605, 2004.

Mertens, C. J., Mlynczak, M. G., López-Puertas, M., Wintersteiner, P. P., Picard, R. H., Winick, J. R., Gordley, L. L., and Russell, J. M.: Retrieval of mesospheric and lower thermospheric kinetic temperature from measurements of CO215 μm Earth Limb Emission under non-LTE conditions, Geophys. Res. Lett., 28, 1391-1394, 10.1029/2000gl012189, 2001.

Mlynczak, M. G., Hunt, L. A., Garcia, R. R., Harvey, V. L., Marshall, B. T., Yue, J., Mertens, C. J., and Russell, J. M., 3rd: Cooling and Contraction of the Mesosphere and Lower Thermosphere From 2002 to 2021, J Geophys Res Atmos, 127, e2022JD036767, 10.1029/2022JD036767, 2022.

Mlynczak, M. G., Marshall, B. T., Garcia, R. R., Hunt, L., Yue, J., Harvey, V. L., Lopez-Puertas, M., Mertens, C., and Russell, J.: Algorithm Stability and the Long-Term Geospace Data Record From TIMED/SABER, Geophys. Res. Lett., 50, 10.1029/2022gl102398, 2023.

https://doi.org/10.5194/egusphere-2025-2610
Preprint. Discussion started: 23 June 2025

Mukhtarov, P., Pancheva, D., and Andonov, B.: Global structure and seasonal and interannual variability of the migrating diurnal tide seen in the SABER/TIMED temperatures between 20 and 120 km, J. Geophys. Res.: Space Phys., 114, n/a-n/a, 10.1029/2008ja013759, 2009.

Newman, P. A., Coy, L., Pawson, S., and Lait, L. R.: The anomalous change in the QBO in 2015-2016, Geophys. Res. Lett., 43, 8791-8797, 10.1002/2016gl070373, 2016.

Neale, R., Richter, J. H., Conley, A. J., Park, S., Lauritzen, P. H., Gettelman, A., Williamson, D., Rasch, P. J., Vavrus, S. J., Taylor, M. A., Collins, W., Zhang, M., & LIN, S. (2010). Description of the NCAR Community Atmosphere Model (CAM 4.0), 10.5065/GSEB-6470, 2010

Oberheide, J., Forbes, J. M., Häusler, K., Wu, Q., and Bruinsma, S. L.: Tropospheric tides from 80 to 400 km: Propagation, interannual variability, and solar cycle effects, J. Geophys. Res.: Atmos., 114, 10.1029/2009jd012388, 2009.

Pedatella, N.: Ionospheric Variability during the 2020–2021 SSW: COSMIC-2 Observations and WACCM-X Simulations, Atmosphere, 13, 10.3390/atmos13030368, 2022.

Pramitha, M., Kishore Kumar, K., Venkat Ratnam, M., Praveen, M., and Rao, S. V. B.: Disrupted Stratospheric QBO Signatures in the Diurnal Tides Over the Low-Latitude MLT Region, Geophys. Res. Lett., 48, 10.1029/2021gl093022, 2021a.

Pramitha, M., Kumar, K. K., Ratnam, M. V., Praveen, M., and Bhaskara Rao, S. V.: Stratospheric Quasi Biennial Oscillation Modulations of Migrating Diurnal Tide in the Mesosphere and Lower Thermosphere Over the Low and Equatorial Latitudes, J. Geophys. Res.: Space Phys., 126, 10.1029/2020ja028970, 2021b.

Qian, L., Emery, B. A., Foster, B., Lu, G., Maute, A., Richmond, A. D., et al.: The NCAR TIE-GCM: A community model of the coupled thermosphere/ionosphere system. In J. Huba, R. Schunk, & G. Khazanov (Eds.), Modeling the ionosphere-thermosphere system, John Wiley, 73–83, 10.1002/9781118704417.ch7, 2014

Sakazaki, T., Fujiwara, M., and Shiotani, M.: Representation of solar tides in the stratosphere and lower mesosphere in state-of-the-art reanalyses and in satellite observations, Atmos. Chem. Phys., 18, 1437-1456, 10.5194/acp-18-1437-2018, 2018.

Santoso, A., McPhaden, M. J., and Cai, W.: The Defining Characteristics of ENSO Extremes and the Strong 2015/2016 El Niño, Rev. Geophys., 55, 1079-1129, 10.1002/2017rg000560, 2017.

Schoeberl, M. R., Douglass, A. R., Newman, P. A., Lait, L. R., Lary, D., Waters, J., Livesey, N., Froidevaux, L., Lambert, A., Read, W., Filipiak, M. J., and Pumphrey, H. C.: QBO and annual cycle variations in tropical lower stratosphere trace gases from HALOE and Aura MLS observations, J. Geophys. Res.: Atmos., 113, 10.1029/2007jd008678, 2008.

Singh, D. and Gurubaran, S.: Variability of diurnal tide in the MLT region over Tirunelveli (8.7°N), India: Consistency between ground- and space-based observations, J. Geophys. Res.: Atmos., 122, 2696-2713, 10.1002/2016jd025910, 2017.

Smith, A. K.: Global Dynamics of the MLT, Surv. Geophys., 33, 1177-1230, 10.1007/s10712-012-9196-9, 2012.

Smith, A. K., Pedatella, N. M., Marsh, D. R., and Matsuo, T.: On the Dynamical Control of the Mesosphere–Lower Thermosphere by the Lower and Middle Atmosphere, J. Atmos. Sci., 74, 933-947, 10.1175/jas-d-16-0226.1, 2017.

Smith, A. K., Harvey, V. L., Mlynczak, M. G., Funke, B., García-Comas, M., Hervig, M., Kaufmann, M., Kyrölä, E., López-Puertas, M., McDade, I., Randall, C. E., Russell, J. M., Sheese, P. E., Shiotani, M., Skinner, W. R., Suzuki, M., and Walker,

https://doi.org/10.5194/egusphere-2025-2610
Preprint. Discussion started: 23 June 2025

K. A.: Satellite observations of ozone in the upper mesosphere, J. Geophys. Res.: Atmos., 118, 5803-5821, 10.1002/jgrd.50445, 2013.

Somerville, R. C. J., Stone, P. H., Halem, M., Hansen, J. E., Hogan, J. S., Druyan, L. M., Russell, G., Lacis, A. A., Quirk, W. J., and Tenenbaum, J.: The GISS Model of the Global Atmosphere, J. Atmos. Sci., 31, 84-117, 10.1175/1520-0469(1974)031<0084:Tgmotg>2.0.Co;2, 1974.

Sun, R., Gu, S., Dou, X., and Li, N.: Tidal Structures in the Mesosphere and Lower Thermosphere and Their Solar Cycle Variations, Atmosphere, 13, 10.3390/atmos13122036, 2022.

Tweedy, O. V., Kramarova, N. A., Strahan, S. E., Newman, P. A., Coy, L., Randel, W. J., Park, M., Waugh, D. W., and Frith, S. M.: Response of trace gases to the disrupted 2015–2016 quasi-biennial oscillation, Atmos. Chem. Phys., 17, 6813-6823, 10.5194/acp-17-6813-2017, 2017.

Vincent, R. A., Kovalam, S., Fritts, D. C., and Isler, J. R.: Long-term MF radar observations of solar tides in the low-latitude mesosphere: Interannual variability and comparisons with the GSWM, J. Geophys. Res.: Atmos., 103, 8667-8683, 10.1029/98jd00482, 1998.

Wang, J., Li, N., Yi, W., Xue, X., Reid, I. M., Wu, J., Ye, H., Li, J., Ding, Z., Chen, J., Li, G., Tian, Y., Chang, B., Wu, J., and Zhao, L.: The impact of quasi-biennial oscillation (QBO) disruptions on diurnal tides over the low- and mid-latitude mesosphere and lower thermosphere (MLT) region observed by a meteor radar chain, Atmos. Chem. Phys., 24, 13299-13315, 10.5194/acp-24-13299-2024, 2024.

Wang, Y., Rao, J., Lu, Y., Ju, Z., Yang, J., and Luo, J.: A revisit and comparison of the quasi-biennial oscillation (QBO) disruption events in 2015/16 and 2019/20, Atmos. Res., 294, 10.1016/j.atmosres.2023.106970, 2023.

Wu, Q., Ortland, D. A., Killeen, T. L., Roble, R. G., Hagan, M. E., Liu, H. L., Solomon, S. C., Xu, J., Skinner, W. R., and Niciejewski, R. J.: Global distribution and interannual variations of mesospheric and lower thermospheric neutral wind diurnal tide: 1. Migrating tide, J. Geophys. Res.: Space Phys., 113, n/a-n/a, 10.1029/2007ja012542, 2008.

Xu, J., Smith, A. K., Jiang, G., and Yuan, W.: Seasonal variation of the Hough modes of the diurnal component of ozone heating evaluated from Aura Microwave Limb Sounder observations, J. Geophys. Res.: Atmos., 115, 10.1029/2009jd013179, 2010.

Xu, J., Smith, A. K., Yuan, W., Liu, H. L., Wu, Q., Mlynczak, M. G., and Russell, J. M.: Global structure and long-term variations of zonal mean temperature observed by TIMED/SABER, J. Geophys. Res., 112, 10.1029/2007jd008546, 2007.

Xu, J., Smith, A. K., Liu, H. L., Yuan, W., Wu, Q., Jiang, G., Mlynczak, M. G., Russell, J. M., and Franke, S. J.: Seasonal and quasi-biennial variations in the migrating diurnal tide observed by Thermosphere, Ionosphere, Mesosphere, Energetics and Dynamics (TIMED), J. Geophys. Res., 114, 10.1029/2008jd011298, 2009.